Damage mechanisms of MoN/SiN multilayer optics for next-generation pulsed XUV light sources

R. Sobierajski,[1,2,*] S. Bruijn,[1] A.R. Khorsand,[1,3] E. Louis,[1] R.W. E. van de Kruijs,[1] T. Burian,[4] J. Chalupsky,[4] J. Cihelka,[4,5] A. Gleeson,[6] J. Grzonka,[7] E.M. Gullikson,[8] V. Hajkova,[4] S. Hau-Riege,[9] L. Juha,[4] M. Jurek,[2] D. Klinger,[2] J. Krzywinski,[10] R. London,[9] J. B. Pelka[2] T. Płociński,[7] M. Rasiński,[7] K. Tiedtke,[11] S. Toleikis,[11] L. Vysin,[4] H. Wabnitz,[11] and F. Bijkerk[1,12]

[1]*FOM-Institute for Plasma Physics Rijnhuizen, Edisonbaan 14, NL-3430 BE Nieuwegein, Netherlands*
[2]*Institute of Physics Polish Academy of Sciences, Al. Lotników 32/46, PL 02-668 Warsaw, Poland*
[3]*currently with the Radboud University Nijmegen, Institute for Molecules and Materials, Netherlands*
[4]*Institute of Physics AS CR, Na Slovance 2, 182 21 Prague 8, Czech Republic*
[5]*J. Heyrovsky Institute of Physical Chemistry ASCR, v. v. i.Dolejškova 2155/3, 182 23 Prague 8, Czech Republic*
[6]*CCRLC Daresbury Laboratory, Warrington, Cheshire, WA4 4AD, UK*
[7]*Warsaw University of Technology, Wołoska 141, PL 02-507 Warsaw, Poland*
[8]*Center for X-Ray Optics, Lawrence Berkeley National Laboratory, Berkeley, California 94720, USA*
[9]*Lawrence Livermore National Laboratory, 7000 East Avenue, Livermore, California 94550, USA*
[10]*SLAC National Accelerator Laboratory, 2575 Sand Hill Road, Menlo Park California 94025, USA*
[11]*Deutsches Elektronen-Synchrotron DESY, Notkestrasse 85, 22607 Hamburg, Germany*
[12]*MESA + Institute for Nanotechnology, University of Twente, Netherlands*
**ryszard.sobierajski@ifpan.edu.pl*

Abstract: We investigated the damage mechanism of MoN/SiN multilayer XUV optics under two extreme conditions: thermal annealing and irradiation with single shot intense XUV pulses from the free-electron laser facility in Hamburg - FLASH. The damage was studied "post-mortem" by means of X-ray diffraction, interference-polarizing optical microscopy, atomic force microscopy, and scanning transmission electron microscopy. Although the timescale of the damage processes and the damage threshold temperatures were different (in the case of annealing it was the dissociation temperature of Mo_2N and in the case of XUV irradiation it was the melting temperature of MoN) the main damage mechanism is very similar: molecular dissociation and the formation of N_2, leading to bubbles inside the multilayer structure.

©2010 Optical Society of America

OCIS codes: (140.3330) Laser damage; (140.6810) Thermal effects; (230.4170) Multilayers; (220.0220) Optical design and fabrication; (140.2600) Free-electron lasers (FELs).

References and links

1. W. Ackermann, G. Asova, V. Ayvazyan, A. Azima, N. Baboi, J. Bahr, V. Balandin, B. Beutner, A. Brandt, A. Bolzmann, R. Brinkmann, O. I. Brovko, M. Castellano, P. Castro, L. Catani, E. Chiadroni, S. Choroba, A. Cianchi, J. T. Costello, D. Cubaynes, J. Dardis, W. Decking, H. Delsim Hashemi, A. Delserieys, G. Di Pirro, M. Dohlus, S. Dusterer, A. Eckhardt, H. T. Edwards, B. Faatz, J. Feldhaus, K. Flottmann, J. Frisch, L. Frohlich, T. Garvey, U. Gensch, C. Gerth, M. Gorler, N. Golubeva, H. J. Grabosch, M. Grecki, O. Grimm, K. Hacker, U. Hahn, J. H. Han, K. Honkavaara, T. Hott, M. Huning, Y. Ivanisenko, E. Jaeschke, W. Jalmuzna, T. Jezynski, R. Kammering, V. Katalev, K. Kavanagh, E. T. Kennedy, S. Khodyachykh, K. Klose, V. Kocharyan, M. Korfer, M. Kollewe, W. Koprek, S. Korepanov, D. Kostin, M. Krassilnikov, G. Kube, M. Kuhlmann, C. L. S. Lewis, L. Lilje, T. Limberg, D. Lipka, F. Lohl, H. Luna, M. Luong, M. Martins, M. Meyer, P. Michelato, V. Miltchev, W. D. Moller, L. Monaco, W. F. O. Muller, O. Napieralski, O. Napoly, P. Nicolosi, D. Nolle, T. Nunez, A. Oppelt, C. Pagani, R. Paparella, N. Pchalek, J. Pedregosa Gutierrez, B. Petersen, B. Petrosyan, G. Petrosyan, L. Petrosyan, J. Pfluger, E. Plonjes, L. Poletto, K. Pozniak, E. Prat, D. Proch, P. Pucyk, P. Radcliffe, H. Redlin, K. Rehlich, M. Richter, M. Roehrs, J. Roensch, R. Romaniuk, M. Ross, J. Rossbach, V. Rybnikov, M. Sachwitz, E. L. Saldin, W. Sandner, H. Schlarb, B. Schmidt, M. Schmitz, P. Schmuser, J. R. Schneider, E. A. Schneidmiller, S. Schnepp, S. Schreiber, M. Seidel, D. Sertore, A. V. Shabunov, C. Simon, S. Simrock, E. Sombrowski, A. A. Sorokin, P. Spanknebel, R. Spesyvtsev, L. Staykov, B. Steffen, F. Stephan, F. Stulle, H. Thom, K. Tiedtke, M. Tischer, S. Toleikis, R. Treusch, D. Trines, I. Tsakov, E. Vogel, T. Weiland, H. Weise, M. Wellhofer, M. Wendt,

#136911 - $15.00 USD Received 20 Oct 2010; revised 9 Dec 2010; accepted 9 Dec 2010; published 22 Dec 2010

I. Will, A. Winter, K. Wittenburg, W. Wurth, P. Yeates, M. V. Yurkov, I. Zagorodnov, and K. Zapfe, “Operation of a free-electron laser from the extreme ultraviolet to the water window,” Nat. Photonics **1**(6), 336–342 (2007).

2. E. Allaria, C. Callegari, D. Cocco, W. M. Fawley, M. Kiskinova, C. Masciovecchio, and F. Parmigiani, “The FERMI@Elettra free-electron-laser source for coherent X-ray physics: photon properties, beam transport system and applications,” N. J. Phys. **12**(7), 075002 (2009).
3. T. Shintake, H. Tanaka, T. Hara, T. Tanaka, K. Togawa, M. Yabashi, Y. Otake, Y. Asano, T. Bizen, T. Fukui, S. Goto, A. Higashiya, T. Hirono, N. Hosoda, T. Inagaki, S. Inoue, M. Ishii, Y. Kim, H. Kimura, M. Kitamura, T. Kobayashi, H. Maesaka, T. Masuda, S. Matsui, T. Matsushita, X. Marechal, M. Nagasono, H. Ohashi, T. Ohata, T. Ohshima, K. Onoe, K. Shirasawa, T. Takagi, S. Takahashi, M. Takeuchi, K. Tamasaku, R. Tanaka, Y. Tanaka, T. Tanikawa, T. Togashi, S. Wu, A. Yamashita, K. Yanagida, C. Zhang, H. Kitamura, and T. Ishikawa, “A compact free-electron laser for generating coherent radiation in the extreme ultraviolet region,” Nat. Photonics **2**(9), 555–559 (2008).
4. P. Balcou, R. Haroutunian, S. Sebban, G. Grillon, A. Rousse, G. Mullot, J. P. Chambaret, G. Rey, A. Antonetti, D. Hulin, L. Roos, D. Descamps, M. B. Gaarde, A. L’Huillier, E. Constant, E. Mevel, D. von der Linde, A. Orisch, A. Tarasevitch, U. Teubner, D. Klöpfel, and W. Theobald, “High-order-harmonic generation: towards laser-induced phase-matching control and relativistic effects,” Appl. Phys, B-Lasers. **74**, 509–515 (2002).
5. S. Kazamias, D. Douillet, F. Weihe, C. Valentin, A. Rousse, S. Sebban, G. Grillon, F. Augé, D. Hulin, and P. Balcou, “Global optimization of high harmonic generation,” Phys. Rev. Lett. **90**(19), 193901 (2003).
6. B. Rus, T. Mocek, A. R. Präg, M. Kozlová, G. Jamelot, A. Carillon, D. Ros, D. Joyeux, and D. Phalippou, “Multimillijoule, highly coherent X-ray laser at 21 nm operating in deep saturation through double-pass amplification,” Phys. Rev. A **66**(6), 063806 (2002).
7. S. Heinbuch, M. Grisham, D. Martz, and J. J. Rocca, “Demonstration of a desk-top size high repetition rate soft x-ray laser,” Opt. Express **13**(11), 4050–4055 (2005).
8. H. N. Chapman, S. P. Hau-Riege, M. J. Bogan, S. Bajt, A. Barty, S. Boutet, S. Marchesini, M. Frank, B. W. Woods, W. H. Benner, R. A. London, U. Rohner, A. Szöke, E. Spiller, T. Möller, C. Bostedt, D. A. Shapiro, M. Kuhlmann, R. Treusch, E. Plönjes, F. Burmeister, M. Bergh, C. Caleman, G. Huldt, M. M. Seibert, and J. Hajdu, “Femtosecond time-delay X-ray holography,” Nature **448**(7154), 676–679 (2007).
9. B. Nagler, U. Zastrau, R. R. Fäustlin, S. M. Vinko, T. Whitcher, A. J. Nelson, R. Sobierajski, J. Krzywinski, J. Chalupsky, E. Abreu, S. Bajt, T. Bornath, T. Burian, H. Chapman, J. Cihelka, T. Döppner, S. Düsterer, T. Dzelzainis, M. Fajardo, E. Förster, C. Fortmann, E. Galtier, S. H. Glenzer, S. Göde, G. Gregori, V. Hajkova, P. Heimann, L. Juha, M. Jurek, F. Y. Khattak, A. R. Khorsand, D. Klinger, M. Kozlova, T. Laarmann, H. J. Lee, R. W. Lee, K.-H. Meiwes-Broer, P. Mercere, W. J. Murphy, A. Przystawik, R. Redmer, H. Reinholz, D. Riley, G. Röpke, F. Rosmej, K. Saksl, R. Schott, R. Thiele, J. Tiggesbäumker, S. Toleikis, T. Tschentscher, I. Uschmann, H. J. Vollmer, and J. S. Wark, “Turning solid aluminium transparent by intense soft X-ray photoionization,” Nat. Phys. **5**(9), 693–696 (2009).
10. A. J. Nelson, S. Toleikis, H. Chapman, S. Bajt, J. Krzywinski, J. Chalupsky, L. Juha, J. Cihelka, V. Hajkova, L. Vysin, T. Burian, M. Kozlova, R. R. Fäustlin, B. Nagler, S. M. Vinko, T. Whitcher, T. Dzelzainis, O. Renner, K. Saksl, A. R. Khorsand, P. A. Heimann, R. Sobierajski, D. Klinger, M. Jurek, J. Pelka, B. Iwan, J. Andreasson, N. Timneanu, M. Fajardo, J. S. Wark, D. Riley, T. Tschentscher, J. Hajdu, and R. W. Lee, “Soft x-ray free electron laser microfocus for exploring matter under extreme conditions,” Opt. Express **17**(20), 18271–18278 (2009).
11. R. Sobierajski, M. Jurek, D. Klinger, J. Krzywinski, J. B. Pelka, H. Chapman, S. P. Hau-Riege, R. London, L. Juha, J. Chalupský, J. Cihelka, K. Tiedtke, S. Toleikis, H. Wabnitz, U. Jastrow, K. Sokolowski-Tinten, and N. Stojanovic, “Evolution of optical properties of surfaces under influence of ultra short pulses of intense EUV radiation,” HASYLAB Annual Report, 395–396 (2006).
12. A. R. Khorsand, R. Sobierajski, E. Louis, S. Bruijn, E. D. van Hattum, R. W. E. van de Kruijs, M. Jurek, D. Klinger, J. B. Pelka, L. Juha, T. Burian, J. Chalupsky, J. Cihelka, V. Hajkova, L. Vysin, U. Jastrow, N. Stojanovic, S. Toleikis, H. Wabnitz, K. Tiedtke, K. Sokolowski-Tinten, U. Shymanovich, J. Krzywinski, S. Hau-Riege, R. London, A. Gleeson, E. M. Gullikson, and F. Bijkerk, “Single shot damage mechanism of Mo/Si multilayer optics under intense pulsed XUV-exposure,” Opt. Express **18**(2), 700–712 (2010).
13. F. Barkusky, A. Bayer, S. Döring, P. Grossmann, and K. Mann, “Damage threshold measurements on EUV optics using focused radiation from a table-top laser produced plasma source,” Opt. Express **18**(5), 4346–4355 (2010).
14. H. Nakajima, M. Ikebe, Y. Muto, S. Yamaguchi, and H. Fujimori, “Diffusion behaviour and superconducting properties of sputtered-deposited Mo/Si and MoN/SiN multilayers,” MRS Int'l. on Adv, Mats. **10**, 405 (1989).
15. E. Louis, H. J. Voorma, N. B. Koster, F. Bijkerk, Y. Y. Platonov, S. Y. Zuev, S. S. Andreev, E. A. Shamov, and N. N. Salashchenko, “Multilayer coated reflective optics for Extreme UV lithography,” Microelectron. Eng. **27**(1-4), 235–238 (1995).
16. E. Louis, H. J. Voorma, N. B. Koster, L. Shmaenok, F. Bijkerk, R. Schlatmann, J. Verhoeven, Y. Y. Platonov, G. E. van Dorssen, and H. A. Padmore, “Enhancement of reflectivity of multilayer mirrors for soft X-ray projection lithography by temperature optimization and ion bombardment,” Microelectron. Eng. **23**(1-4), 215–218 (1994).
17. E. Louis, A. E. Yakshin, P. C. Goerts, S. Oestreich, R. Stuik, E. L. G. Maas, M. J. H. Kessels, F. Bijkerk, M. Haidl, S. Muellender, M. Mertin, D. Schmitz, F. Scholze, and G. Ulm, “Progress in Mo/Si multilayer coating technology for EUVL optics,” SPIE 406–411 (2000).
18. H. J. Voorma, E. Louis, F. Bijkerk, and S. Abdali, “Angular and energy dependence of ion bombardment of Mo/Si multilayers,” J. Appl. Phys. **82**(4), 1876–1881 (1997).
19. R. Kärcher, L. Ley, and R. L. Johnson, “Electronic structure of hydrogenated and unhydrogenated amorphous SiNx ($0 \leq x \leq 1.6$): A photoemission study,” Phys. Rev. B **30**(4), 1896–1910 (1984).

#136911 - $15.00 USD Received 20 Oct 2010; revised 9 Dec 2010; accepted 9 Dec 2010; published 22 Dec 2010
(C) 2011 OSA

20. I. Kusunoki, T. Takaoka, Y. Igari, and K. Ohtsuka, “Nitridation of a Si(100) surface by 100–1000 eV N^{+2} ion beams,” J. Chem. Phys. **101**(9), 8238–8245 (1994).
21. E. P. Donovan, G. K. Hubler, M. S. Mudholkar, and L. T. Thompson, “Ion-beam-assisted deposition of molybdenum nitride films,” Surf. Coat. Tech. **66**(1-3), 499–504 (1994).
22. D. L. Windt, “IMD - Software for modeling the optical properties of multilayer films,” Comput. Phys. **12**(4), 360–370 (1998).
23. K. Tiedtke, A. Azima, N. von Bargen, L. Bittner, S. Bonfigt, S. Düsterer, B. Faatz, U. Frühling, M. Gensch, C. Gerth, N. Guerassimova, U. Hahn, T. Hans, M. Hesse, K. Honkavaar, U. Jastrow, P. Juranic, S. Kapitzki, B. Keitel, T. Kracht, M. Kuhlmann, W. B. Li, M. Martins, T. Núñez, E. Plönjes, H. Redlin, E. L. Saldin, E. A. Schneidmiller, J. R. Schneider, S. Schreiber, N. Stojanovic, F. Tavella, S. Toleikis, R. Treusch, H. Weigelt, M. Wellhöfer, H. Wabnitz, M. V. Yurkov, and J. Feldhaus, “The soft X-ray free-electron laser FLASH at DESY: beamlines, diagnostics and end-stations,” N. J. Phys. **11**(2), 023029 (2009).
24. K. Tiedtke, J. Feldhaus, U. Hahn, U. Jastrow, T. Nunez, T. Tschentscher, S. V. Bobashev, A. A. Sorokin, J. B. Hastings, S. Moller, L. Cibik, A. Gottwald, A. Hoehl, U. Kroth, M. Krumrey, H. Schoppe, G. Ulm, and M. Richter, “Gas detectors for X-ray lasers,” J. Appl. Phys. **103**(9), 094511 (2008).
25. S. P. Hau-Riege, R. A. London, H. N. Chapman, and M. Bergh, “Soft-x-ray free-electron-laser interaction with materials,” Phys. Rev. E Stat. Nonlin. Soft Matter Phys. **76**(4), 046403 (2007).
26. J. Chalupský, L. Juha, J. Kuba, J. Cihelka, V. Hájková, S. Koptyaev, J. Krása, A. Velyhan, M. Bergh, C. Caleman, J. Hajdu, R. M. Bionta, H. Chapman, S. P. Hau-Riege, R. A. London, M. Jurek, J. Krzywinski, R. Nietubyc, J. B. Pelka, R. Sobierajski, J. Meyer-Ter-Vehn, A. Tronnier, K. Sokolowski-Tinten, N. Stojanovic, K. Tiedtke, S. Toleikis, T. Tschentscher, H. Wabnitz, and U. Zastrau, “Characteristics of focused soft X-ray free-electron laser beam determined by ablation of organic molecular solids,” Opt. Express **15**(10), 6036–6043 (2007).
27. J. M. Liu, “Simple technique for measurements of pulsed Gaussian-beam spot sizes,” Opt. Lett. **7**(5), 196–198 (1982).
28. D. L. Lide, ed., *CRC Handbook of Chemistry and Physics,* 90th Edition (2009–2010).
29. R. W. E. van de Kruijs, E. Zoethout, A. E. Yakshin, I. Nedelcu, E. Louis, H. Enkisch, G. Sipos, S. Mullender, and F. Bijkerk, “Nano-size crystallites in Mo/Si multilayer optics,” Thin Solid Films **515**(2), 430–433 (2006).
30. I. Nedelcu, R. W. E. van de Kruijs, A. E. Yakshin, and F. Bijkerk, “Thermally enhanced interdiffusion in Mo/Si multilayers,” J. Appl. Phys. **103**(8), 083549 (2008).
31. D. Attwood, *Soft X-rays and Extreme Ultraviolet Radiation - Principles and Applications* (Cambridge University Press, Cambridge, 1999).
32. PDF card number 25–1366.
33. A. L. Patterson, “The Scherrer Formula for X-Ray Particle Size Determination,” Phys. Rev. **56**(10), 978–982 (1939).
34. PDF card number. 25–1368.
35. H. Jehn, and P. Ettmayer, “The molybdenum-nitrogen phase diagram,” J. Less Common Met. **58**(1), 85–98 (1978).
36. K. Frisk, “A thermodynamic evaluation of the Cr-N, Fe-N, Mo-N and Cr-Mo-N systems,” Calphad **15**(1), 79–106 (1991).

1. Introduction

The rapid development of a new generation of extreme ultraviolet (XUV) radiation sources providing ultra-short (from atto- to nanoseconds) pulses creates new challenges for optics. Instruments, like free-electron lasers (FELs) [1–3], higher harmonic generating sources (HHG) [4, 5], high-energy coherent sources based on laser plasmas [6], and capillary discharge lasers [7] produce pulses of very high intensity which may induce radiation damage in optical coatings. Two damage mechanisms are of special importance: (a) permanent damage of the coatings due to structural changes and (b) change of the optical properties of materials under high intensity XUV irradiation. They are new compared to the ones observed in the previous generation of light sources, like plasma sources used in lithography or synchrotrons. Both mechanisms may be a limiting factor for many scientific and industrial applications. Therefore, for a proper design of optics for current and future XUV light sources, it is crucial to understand the physical mechanisms leading to radiation damage.

It is especially important for multilayer coated mirrors where, at the resonant angle, the absorbed energy density is the highest. They are widely used in “front-line” experiments like XUV time resolved holography as a part of the imaging system [8], as diffraction limited XUV beam focusing optics for warm dense matter creation [9, 10] and as a part of the delay line for one color pump and probe studies on XUV transmission of solids [11]. Recently, the single shot damage mechanism in one type of these optical coatings – the Mo/Si multilayer – was studied [12, 13] at the FLASH (Free-electron LASer in Hamburg) facility (providing fs XUV pulses) and using an XUV plasma source at the Laser Lab Goettingen, Germany (with

#136911 - $15.00 USD Received 20 Oct 2010; revised 9 Dec 2010; accepted 9 Dec 2010; published 22 Dec 2010
(C) 2011 OSA

ns pulse duration). Melting of amorphous Si layers followed by diffusion of Mo atoms into the molten Si and subsequent molybdenum silicide formation was proved to be the leading damage mechanism in these multilayers. To block this damage processes, one should use materials with high melting points and with low diffusion constants, preventing intermixing of the layers. These conditions are fulfilled by MoN/SiN multilayers. They have melting temperatures of the individual layers higher than silicon. Moreover, below the temperature that one of the compounds melts, the atomic diffusion coefficient in MoN/SiN multilayer is 11 orders of magnitude lower than in Mo/Si multilayers [14].

The goal of the current paper is to determine the damage threshold and the damage mechanism for MoN/SiN multilayers exposed to an intense ultrashort pulse of XUV radiation. The results are compared to the damage caused by thermal annealing of the multilayers.

2. Experimental

The MoN/SiN multilayer coatings used in this work have been deposited on superpolished Si substrates using e-beam evaporation of Mo atoms and magnetron sputtering of Si atoms in a UHV background of 1×10^{-8} mbar, with post-deposition smoothing using low energy ion treatment of the Si layers [15–18]. Nitridation of the Mo and Si layers was achieved by low energy nitrogen ion treatment during deposition [19–21]. X-ray photo-electron spectroscopy (XPS) was used to qualify the nitridation process. E-beam deposition of Mo layers was selected due to the higher quality nitride. XPS shows atomic concentration ratios between Mo and N and Si and N that were both equal to 1 ± 0.1, signifying MoN and SiN formation. Since the most common stoichiometry for silicon nitride is Si_3N_4, the nitridation of the Si was not saturated.

The as-deposited sample was further characterized by means of hard X-ray (λ = 0.15406 nm) and XUV reflectometry. The first technique provides information on the layered structure, including layer thicknesses and multilayer period. The latter technique determines the multilayer performance, i.e. the angular resolved reflectivity of the multilayer for s-polarized light at 13.5 nm for low (non-destructive) irradiation intensities. From these measurements, the performance of the multilayer for any polarization and angle can then be predicted by means of simulations with the software package IMD [22]. The multilayer consisted of 40 bilayers of MoN and SiN, with a periodicity of 8.18 nm and a MoN layer thickness of 40% of the total thickness. The resonant angle and maximum reflectance for 90% s-polarized light were determined to be 27 degrees off-normal incidence and 26.5%, respectively (see Fig. 1).

The sample was irradiated at the FLASH facility in Hamburg, Germany [1, 23]. The radiation wavelength was 13.45 ± 0.05 nm and the XUV pulse duration was in the order of 10 fs (FWHM). The sample was aligned at resonant angle with respect to the incident photon beam which was p-polarized. Since the pulse energy fluctuated from pulse to pulse in the range of 0.01 – 1 μJ it was measured with a gas monitor detector [24]. The radiation was focused with a grazing incidence carbon-coated ellipsoidal mirror at the focal length of 2 m. The footprint of the beam on the sample had an area at 1/e intensity level of 66 ± 3 μm^2. To obtain a Gaussian beam shape, a 3 mm diameter circular aperture in front of the focusing mirror was used. Most of the experiments were performed in "high intensity" mode, with the sample in the focus of the beam. For the given energy fluctuation, this mode corresponded to a beam fluence range of ~15 – 1500 mJ/cm^2. In addition, for the purpose of reflectance studies, measurements at lower intensities were performed with the sample placed ~70 mm out of focus, corresponding to a ~15000 μm^2 footprint area at 1/e intensity level and a fluence range of approx. 0.05 – 5 mJ/cm^2 for the same energy range. The sample was irradiated in single shot mode, i.e., after each irradiation the sample was moved and was irradiated at an unperturbed position. The reflected radiation intensity was measured with a photodiode [12].

After exposing the MoN/SiN sample to the XUV pulses, the irradiated spots were investigated with different techniques: optical microscopy with differential interference contrast - DIC (with Nomarski prism) sensitive to changes of the morphology and optical

#136911 - $15.00 USD Received 20 Oct 2010; revised 9 Dec 2010; accepted 9 Dec 2010; published 22 Dec 2010
(C) 2011 OSA

properties of the materials, atomic force microscopy (AFM) providing a 2D depth map, scanning electron microscopy (SEM) showing the morphology of irradiated spots and, cross-sectional scanning transmission electron microscopy (STEM) to analyze the structural changes below the irradiated surface.

In order to get better insight in the thermal behavior of the MoN/SiN multilayer, a sample from the same coating run was sequentially thermally annealed at 3 different temperatures. The sample was heated to 773 K, 973 K and 1173 K in a vacuum furnace ($<10^{-5}$ mbar). In each step the sample was annealed for a period of 30 minutes. In order to investigate the structure of the layers, the samples were characterized at each temperature with wide angle X-ray diffraction (WAXRD) and grazing incidence X-ray reflection (GIXR). In case of the sample annealed at the highest temperature the surface morphology and internal structure were investigated by means of AFM and STEM scans, respectively.

3. Results

3.1. Reflectometry

XUV reflectivity measurements were carried out using 13.5 nm radiation in three different intensity regimes. The reflectivity at low-intensity (well below the expected damage threshold) was measured at the Center for X-Ray Optics (CXRO) at Berkeley, USA, using 90% s-polarized radiation from the Advance Light Source (ALS), for angles ranging from 10° - 50° off-normal. These measured values were transformed to p-polarized radiation by means of IMD [22] simulations. The reflectivity curve and the IMD simulation for 90% s-polarized light as well as the results for p-polarized light are shown in Fig. 1. The reflectivity measurements at middle and high intensities were performed at FLASH at 28.2 ± 0.3° off-normal. The reflectivity of p-polarized radiation at this angle is shown in Table 1 for all three intensity regimes. The reflectivity is constant, within the error-bars, over the entire intensity-range investigated, i.e. from 100 W/cm^2 to approximately 5×10^{13} W/cm^2, which corresponds to fluences up to 500 mJ/cm^2. This indicates that the damage that is caused by high intensity femtosecond pulses, is not affecting the reflection during the pulse itself and occurs on timescales longer than the pulse duration. This is in agreement with theoretical models [25], where significant change of the optical properties of femtosecond duration pulses is predicted only for fluences above 20 J/cm^2.

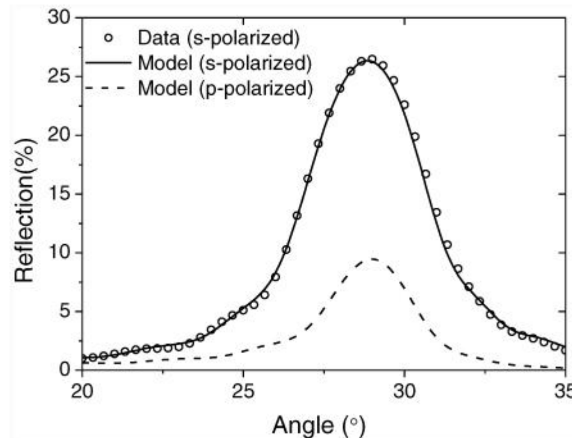

Fig. 1. Reflectivity curve for 90% s-polarized light (λ=13.5 nm), including a model simulation using IMD. Applying the same model, the expected reflectivity for p-polarized radiation is calculated.

#136911 - $15.00 USD Received 20 Oct 2010; revised 9 Dec 2010; accepted 9 Dec 2010; published 22 Dec 2010
(C) 2011 OSA

Table 1: Reflectivity of a MoN/SiN multilayer, at 28.2±0.3° off-normal incidence for 13.5 nm p-polarized radiation.

Facility	Mean intensity [W/cm^2]	Reflectivity [%]
ALS at CXRO	1×10^{2}	7.7 ± 1.0
FLASH (low-intensity regime)	1×10^{11}	7.0 ± 0.2
FLASH (high-intensity regime)	5×10^{13}	6.9 ± 0.3

3.2. Optical microscopy with differential interference contrast

Of each irradiated spot an image was made with a DIC optical microscope. For the purpose of the initial analysis, the damage was defined as the radiation-induced surface changes observable in the image. In Fig. 2 the damaged area is plotted as a function of the logarithm of the pulse energy (blue markers). The single shot damage threshold, which is determined [26, 27] from the intersection of the line fitted to the experimental data points with the x-axis, is equal to 48 ± 7 mJ/cm^2.

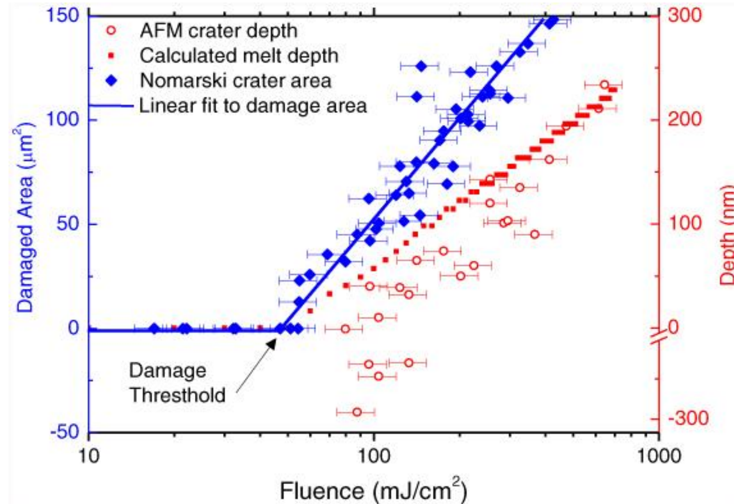

Fig. 2. (Color online) Dependency of the damaged area/depth on the incident beam fluence. The damaged area (blue solid diamonds) was measured by DIC microscopy while the depth of the craters (open red circles) was determined by AFM. The negative values of the AFM correspond to the height of the hills; the depth-axis has been compressed for the negative values. The calculated melt depth (red squares) corresponds to the melting of MoN layers, assuming an averaging of the temperature over each bilayer shortly after energy deposition (see text for details).

3.3. Atomic force microscopy

The morphology of the MoN/SiN multilayer surface after irradiation was further investigated with AFM. Example pictures of three types of observed damage are shown in Fig. 3 (a-c). At low fluences, from the damage threshold up to approximately 100 mJ/cm^2, smooth hills are formed (a). The heights of these hills were between 1 nm and 200 nm. For fluences above 140 mJ/cm^2, a crater is formed which is surrounded by side walls (c). Both the depth of the crater and the dimensions of the wall increase with increasing fluence. The crater's depth varies between 50 nm and 250 nm while the walls height ranges between 40 and 400 nm with an approximately constant width of 1.5 µm. In contrast to the very smooth surface of the hill in the first stages of damage, the wall structure is very rough. In some of the irradiated spots a small hill of about 10 nm height is observed at the bottom of the crater. In an intermediate intensity region, for fluences between 100 and 140 mJ/cm^2 the damage spot consists of a large hill (>100 nm), which is surrounded by a small side wall (b).

The fluence dependency of the depth of the craters and the height of the hills (negative values) is plotted in Fig. 2. In case of the spots from the intermediate intensity regime, both

#136911 - $15.00 USD Received 20 Oct 2010; revised 9 Dec 2010; accepted 9 Dec 2010; published 22 Dec 2010
(C) 2011 OSA

the depth of the crater and the height of the hills are presented. The damage threshold was calculated similarly as for optical microscopy. In case of the AFM data it is equal to 80 ± 13 mJ/cm^2, which is higher than the one obtained from the DIC microscopy data. This difference will be addressed in section 3.5

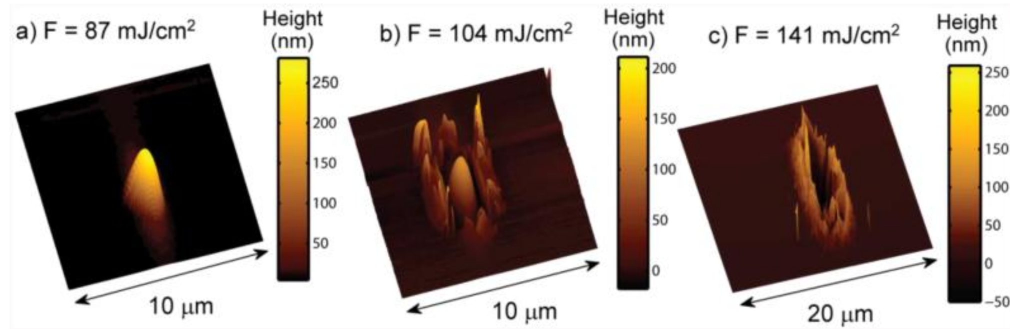

Fig. 3. (Color online) AFM images illustrating the characteristic surface morphology of the multilayer irradiated at three fluence regimes. Just above the damage threshold we observe a smooth hill (a). At intermediate fluences a hill and a crater with side walls can be observed (b). At high fluences, only a crater with high side walls is observed (c).

3.4. Scanning electron microscopy and scanning transmission electron microscopy

One of the spots, exposed to a fluence of 141 mJ/cm^2 (the same as presented in Fig. 3c), was further studied by scanning electron microscopy. The SEM image (Fig. 4) shows that on the edge of the crater many semidetached layers are stacked over each other. They form the wall observed in the AFM map in Fig. 3c. The STEM technique was used to analyze the structural changes below that crater. A thin tungsten layer was deposited on the crater area as a protective layer (and can be seen in Fig. 5a as a black layer on top of the multilayered structure). Next, a 60 nm thin cross-section along the white line marked in the SEM picture (Fig. 4), was made by means of a focused ion beam (FIB). For high resolution images this slab was thinned by low energy argon ion beam polishing. STEM images at different positions with respect to the crater borders were registered with variable magnifications. The results are shown in Fig. 5.

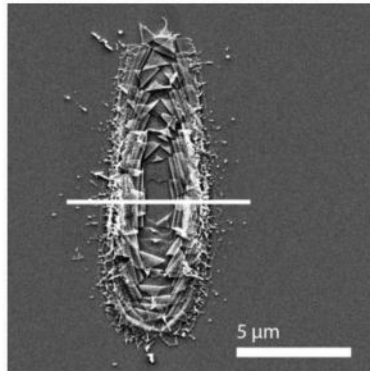

Fig. 4. SEM picture of the crater crated by irradiation with a fluence of 141 mJ/cm^2. The crater is surrounded by partially detached layers positioned over each other. The white line indicates the location for the cross-section STEM pictures in Fig. 5.

#136911 - $15.00 USD Received 20 Oct 2010; revised 9 Dec 2010; accepted 9 Dec 2010; published 22 Dec 2010
(C) 2011 OSA

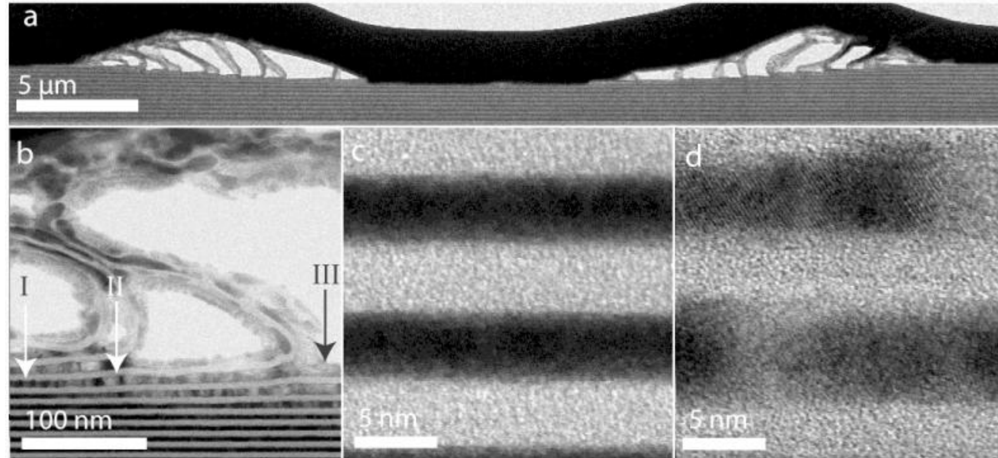

Fig. 5. STEM images of the sample cross-section below the irradiated spot: (a) an overview of the crater, (b) magnified image of one of the pillars, (c) and (d) magnified images of the undamaged and the first stages of damage, respectively. The darker areas correspond to MoN and the lighter areas correspond to SiN. On image (b) three regions are marked (see text for details)

In Fig. 5a an overview image of the crater is shown. The undamaged part of the multilayer can be seen at the bottom of the figure. Above this area we observe structures consisting of pillars of peeled off layers with holes in between (white areas). There is a sharp boundary between the undamaged multilayer and the area where the layers have been peeled off. In Fig. 5b a magnified area of one of the pillars is presented. Due to the transversal distribution of the pulse intensity, the absorbed energy density increases from left to right in the picture. At the lowest fluence, at the location indicated by the arrow I in Fig. 5b, no damage can be observed. At increased fluences, (at location II) new features appear; light areas in the dark MoN layer. Since STEM was used in the bright mode, the white areas indicate that the layer has crystallized. In addition to the crystallization, the MoN layer also expands. The expansion continues until the MoN layer completely delaminates from the underlying multilayer, which can be seen at location III. Magnified images of the multilayer far away from the crater and in close proximity of the crater are shown on Fig. 5c and Fig. 5d, respectively. The crystallization and expansion of the MoN near the crater can be clearly seen in this comparison. In contrast to the changes observed in the MoN layers after exposure, the SiN layer appears to stay intact and forms pillars in between the holes.

3.5. Modeling of molten volume

To further explore the mechanisms responsible for the damage, we addressed the thermal aspects directly after exposure. We estimated the fluence dependent number of the melted MoN layers. The calculations consist of 3 steps. In the first one the depth profile of the energy deposited (absorbed radiation) in the multilayer is calculated. Next it is assumed (in a simplified model) that the heat transfer leads to a temperature equalization over each bilayer. The corresponding temperature profile can be calculated based on the deposited energy density and material constants. The temperature profile is then compared to the melting temperature of the MoN layer and the melted depth (number of bilayers in which MoN is melted) is calculated.

Due to the radiation absorption energy is deposited in the multilayer. The optical flux absorbed at a given depth is proportional to the product of the local field intensity, the real part of the refractive index, and the absorption coefficient. The field intensity can be calculated using IMD software for a given multilayer structure model and radiation fluence. The optical constants can also be obtained from IMD. As a result the depth profile of the absorbed energy density can be obtained as a function of the radiation fluence.

#136911 - $15.00 USD Received 20 Oct 2010; revised 9 Dec 2010; accepted 9 Dec 2010; published 22 Dec 2010
(C) 2011 OSA

Because of a non-uniform energy absorption in the multilayer, the initial temperature is unequally distributed over the bilayers, with maxima in the MoN layers. However, due to strong temperature gradients and heat exchange between the layers, the temperature profile gets smoothened very rapidly. This process is much faster than the heat dissipation to the substrate, due to the much higher temperature gradient. Therefore, it may be considered that shortly after the pulse the temperature is approximately constant over the entire bilayer. The corresponding temperature profile can be calculated from the deposited energy density (averaged over each bilayer) and thermodynamical properties of the materials. Since the thermodynamic constants of SiN and MoN are unknown, the enthalpy of SiN is approximated by the one of Si_3N_4. The enthalpy per MoN molecule is approximated by the enthalpy of only the molybdenum atoms. The contributions of the nitrogen atoms and the atomic interactions are neglected. Since nitrogen atoms are much lighter than Mo atoms, such an approximation seems to be valid, although it may lead to an overestimation of the temperature in the MoN layers.

The calculated temperature can be compared with the melting temperature of each material - the melting temperatures of both MoN and Si_3N_4 are known from literature [28] to be 2023K and 2173 K respectively. The layers which temperature rises above that threshold are considered to melt after irradiation.

From the above described model, the number of molten MoN layers can be calculated. In Fig. 2 (red solid squares) we present the position of the deepest molten MoN layer. The depth of the craters as measured by AFM can be correlated (see Fig. 2) to the number of molten MoN layers (assuming delamination of all the molten layers). The data correspond to each other for fluences above 300 mJ/cm^2. For lower fluences the AFM measured crater depths are lower than the calculated molten depths. This difference can be partly explained by an underestimation of the crater depth for low fluences caused by the hills observed in the center of the crater. Moreover, the STEM data show that one or two layers below the crater do not delaminate and only crystallites are formed within them after irradiation. However the DIC technique is sensitive not only to morphological changes of the material (as AFM) but also structural ones, including formation of the crystallized MoN layer. The damage threshold found from the optical microscopic studies is approximately the same as the melting threshold resulting from the simulations.

3.6. Thermal annealing

In order to obtain a better understanding of the thermal behavior of MoN/SiN multilayers we have sequentially annealed the MoN/SiN multilayer at three different temperatures, 773K, 973 K and 1173 K for 30 minutes. After each exposure the crystallinity and the period of the multilayer were determined by WAXRD and GIXR respectively, at a wavelength of 0.15406 nm; the measurement geometries which were used are exactly the same as the ones discussed in ref [29, 30]. From the GIXR spectra, the period of the multilayer at each annealing step was determined by fitting the Bragg peak positions with the modified Bragg law [31]. From the as deposited state to the state upon annealing to 773 K the period increased by 0.09 nm, which is attributed to expansion in the SiN layer. In the next step, annealing to 973K, the period did not change. At 1173 K the GIXR spectrum did not provide an accurate measure of the period anymore, the reason for this will be discussed below.

The results of the WAXRD measurements are shown in Fig. 6, the diffraction pattern of the reference spectrum is identified as tetragonal Mo_2N (β-Mo_2N [32],), as indicated with the dotted lines and the Miller indices on the top of the graph. Apparently, already at room temperature, randomly oriented polycrystalline Mo_2N crystallizes inside the layer. Since the deposited ratio between Mo and N is 1:1, the excess of N must be incorporated in the uncrystallized part of the layer or diffuse towards the SiN layer. During annealing to 773 K the WAXRD peaks become sharper, and all the peaks shift to higher angles. The sharper peaks indicate an increase in crystallite size [33], the peak shifts are caused by an isotropic contraction of the lattice parameters. In the next step, annealing to 973 K, the WAXRD spectrum does not change significantly, except for a small shift of the (111) peak. At 1173K,

#136911 - $15.00 USD Received 20 Oct 2010; revised 9 Dec 2010; accepted 9 Dec 2010; published 22 Dec 2010
(C) 2011 OSA

the spectrum shows two additional peaks and a large change in the (111) peak. The two new peaks, at 95° and 99°, can be attributed to cubic Mo_2N (γ-Mo_2N [34],). The reference peak positions of this crystalline phase are indicated with dashed lines and Miller indices, as well. The peak shift of the (111) peak at 973 K can be attributed to the start of the transformation to γ-Mo_2N.

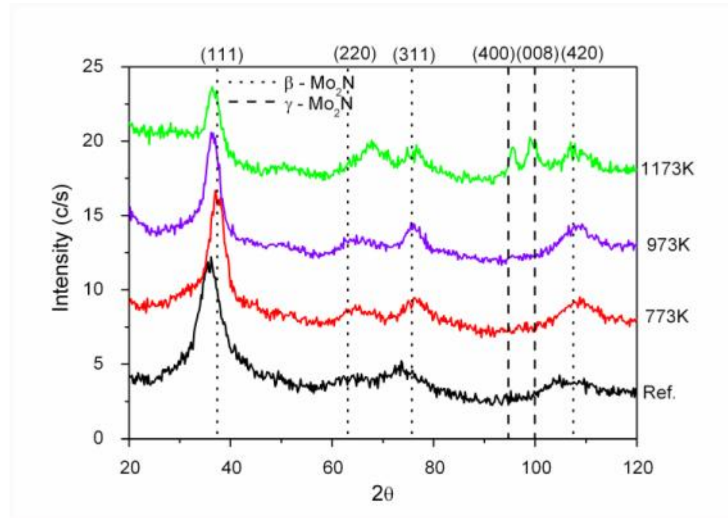

Fig. 6. (Color online) XRD spectra from a MoN/SiN multilayer taken before annealing, and after annealing at 773K, 973K, and 1173K. Every data set is plotted with an offset of 5 counts for clarity.

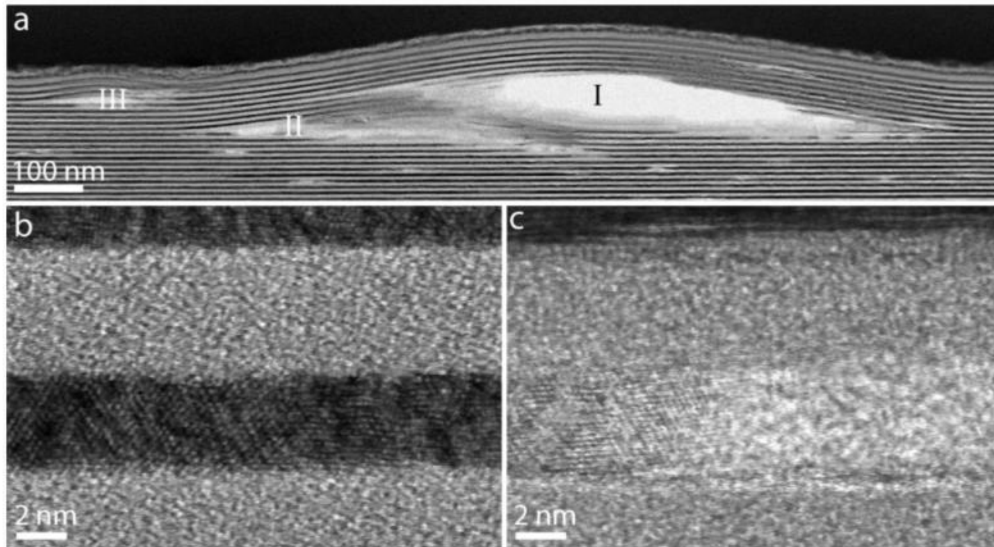

Fig. 7. STEM images of the multilayer annealed to 1173K. (a) Example of three bubbles, marked with I-III. (b) Magnified image of the highly ordered crystalline structure present in most of the MoN layers. (c) Magnified image of an amorphous, low density, structure that can be found at various locations in the MoN layers.

After annealing to 1173K, AFM investigations showed the formation of hills all over the multilayer surface, which were not present at 773 K and 973 K. The hills vary in height from 6 to 70 nm and in width at their base from 0.2 to 1 µm. Further cross-sectional STEM was performed on the multilayer annealed at 1173K. In Fig. 7a it is shown that the hills are caused

#136911 - $15.00 USD Received 20 Oct 2010; revised 9 Dec 2010; accepted 9 Dec 2010; published 22 Dec 2010
(C) 2011 OSA

by bubble formation inside the multilayer (I-III). Apart from the bubbles, structural changes are also observed inside the MoN layers, one of which is magnified in Fig. 7c. They are amorphous and, since they appear very light in the STEM picture, have a lower density. Most likely these are the onset of the formation of bubbles. At all the other positions in the MoN layers we observe highly ordered crystallites (Fig. 7b). The macroscopic roughness introduced by these bubbles explains why we were not able to determine the period with GIXR at this temperature.

4. Discussion

The MoN/SiN multilayer was exposed to two different extreme conditions: thermal annealing and single shot fs-XUV laser pulse irradiation at the FLASH facility. Although the main parameters of the exposures (timing, temperature and lateral distribution of the absorbed heat) were completely different, similarities in the mechanisms responsible for damage in the multilayer were observed. In both cases crystallization of the MoN layer and the formation of bubbles in the MoN layer are the main cause of damage.

The as-deposited state of the MoN layers in the studied samples is mostly an amorphous mix of Mo and N atoms in a ratio of 1:1. In between the MoN a small amount of β-Mo_2N crystals have formed. When the temperature was raised during annealing, the WAXRD spectra showed that the Mo_2N crystallites increase in size. At 1173 K the pattern of γ-Mo_2N appears and the AFM and STEM results reveal bubble formation in the structure. The Gibbs free energy of Mo_2N formation in the reaction $Mo(s) + N_2(g) \rightleftharpoons Mo_2N(s)$ for an N_2 pressure of 1 bar can be written as [35]:

$$\Delta G^0_{Mo_2N} = -57320 + 53.89T, \quad (1)$$

where $\Delta G^0_{Mo_2N}$ is expressed in J/mol and T is the temperature in Kelvin. Mo_2N formation is energetically favorable up to the (dissociation) temperature of 1063 K [28]. This temperature can increase with increasing pressure or concentration of N_2 [35]. In the annealing experiment at 773 K and 973 K, below the dissociation temperature, Mo_2N crystals are formed. After annealing to 1163K, well above the dissociation temperature, the Mo_2N crystallites start to dissociate into Mo and N_2 gas. This process saturates due to the increase of the nitrogen concentration. However, as observed in the STEM images, at some positions the dissociation process leads to formation of volumes of clearly lower density due to a small amount of released N_2 gas. They are the onsets of the bubble formation. At some of them, where there is a “weak point” in the multilayer structure, the MoN layer breaks apart and the SiN layers delaminate, what leads to the formation of bubbles. The development of a bubble decreases the N_2 concentration and more gas can be released due to the further dissociation.

In the case of FLASH, we do not observe any damage or significant crystallization below the melting point of MoN. Atoms simply do not have enough mobility in the solid phase and cannot move over significant distances in the short period that the irradiated area is at an enhanced temperature (it can be assumed that the heat conductance to the Si substrate cools the sample down to room temperature in a time shorter than 1 μs). Above the melting point of MoN, atoms are much more mobile in the liquid MoN phase. STEM images show that crystals are formed at the edge of the melted area and bubbles develop closer to the surface. In line with the annealing results, it is likely that the Mo_2N crystals are formed and N_2 gas is released what leads to bubble formation. However, at the temperatures and multilayer composition used in this study, the phase diagram is not well known [35, 36]. Therefore, the mechanisms of the formation of the N_2 bubbles and the Mo_2N crystals inside the MoN layers cannot be determined with absolute certainty. We propose two different models here. The common starting point for both of them is melting of MoN layer followed by heat dissipation to the substrate and layer solidification.

In the first model we presume that during solidification of MoN the temperature is above the dissociation temperature and therefore Mo_2N cannot form, only solid Mo and N_2 gas. At

#136911 - $15.00 USD Received 20 Oct 2010; revised 9 Dec 2010; accepted 9 Dec 2010; published 22 Dec 2010
(C) 2011 OSA

the edge of the molten volume, the heat dissipation is faster due to the direct thermal contact with cooler layers below. Therefore an under-cooled liquid may form at the edges of the damaged volume. The temperature of this under-cooled liquid can drop below the dissociation temperature of Mo_2N (which can be enhanced due to high nitrogen concentrations). Thus, the thermodynamically favorable, Mo_2N crystals will form there.

In the second model we presume that the dissociation of Mo_2N *cannot* occur due to the very high concentration of nitrogen, higher than the eutectic concentration. Due to the difference in stoichiometry between the Mo_2N crystals and molten MoN phase the extra nitrogen must be released. Since the solvability of the nitrogen in liquid MoN is much higher than in Mo_2N, the N_2 is pushed away from crystals and dissolves in liquid. Thus in the final state, after cooling, there are Mo_2N crystals surrounded by gaseous N_2. The more time the solidification process takes, the bigger crystals are formed (in Fig. 5b the crystal size increases with increasing initial temperature). At the same time the concentration of N_2 in the liquid increases, which results in higher pressure in the bubbles after the solidification process ends. Since the main direction of the heat dissipation is towards the substrate, the deeper layers need less time to solidify what explains formation of small crystals below the crater (see Fig. 4b).

In both models, at the final state, the SiN layers have delaminated due to release of N_2 gas. At fluences just above the damage threshold, the SiN layer stays intact on top of the bubble (Fig. 3), at higher fluences, more N_2 is released, therefore the pressure on the SiN layers becomes to high and the bubble 'bursts' and the SiN layers fall back on the substrate (Fig. 3c and Fig. 4).

Finally we compare the results for MoN/SiN multilayers to those of Mo/Si multilayers. It is remarkable for the MoN/SiN structure of the multilayer the damage threshold (48 ± 7 mJ/cm^2) is almost the same as that of Mo/Si multilayer (45 ± 7 mJ/cm^2), reported earlier [12]. It is partly related to the optical properties of both coatings. The reflection of the Mo/Si multilayer is $42 \pm 1\%$, while the reflectance of the MoN/SiN multilayer is $7 \pm 1\%$. The lower reflectance leads to enhanced absorption in the presently studied case, which causes the temperatures in the materials to be higher. Therefore, the increased melting temperature of MoN and SiN compared to the one of Si is not sufficient to increase the damage threshold. On the other hand the decreased atomic diffusivity [14] in the studied sample below the melting temperature increased the critical temperature in the annealing experiment, compared to the Mo/Si multilayer. Thus, concluding, compared to Mo/Si multilayer the MoN/SiN coatings are expected to have higher damage threshold when expressed as a function of temperature for relatively slow heating processes, but a similar threshold single shot damage threshold in terms of laser energy.

5. Summary and conclusions

We have investigated the damage mechanism of MoN/SiN multilayers resulting from two potential damage processes: continuous thermal annealing and single shot irradiation with femtosecond XUV pulses at the FLASH facility. In the case of thermal annealing, the formation of Mo_2N crystals in the MoN layer occurs below 1063K. Above this temperature, the MoN layer dissociates into Mo and gaseous N_2 which agglomerates in the form of bubbles in the multilayer materials. In case of the XUV laser irradiations, permanent damage of the multilayer occurs on a much longer timescale than the pulse duration and, consequently, does not affect the reflection process during the pulse. The single-shot damage threshold of the multilayer is determined to be 48 ± 7 mJ/cm^2. At this fluence the MoN layer reaches the melting temperature. "Post-mortem" studies of the multilayer show that crystals form at the edge of the melted area and bubbles develop closer to the multilayer surface. Since the thermodynamical data are not available for the atomic concentrations and temperatures studied, we propose two possible models describing the XUV damage process. Both lead to the release of the excess N_2 which forms bubbles in the multilayer structure, but they differ by the role of the dissociation process. In the first model MoN decomposition is the key process and in the second model such decomposition is blocked by the saturating nitrogen

#136911 - $15.00 USD Received 20 Oct 2010; revised 9 Dec 2010; accepted 9 Dec 2010; published 22 Dec 2010
(C) 2011 OSA

concentration, but due to the difference in stochiometry between the Mo_2N crystals and molten MoN phase the extra nitrogen must be released.

Although the main parameters of the exposure (timing, temperature and lateral distribution of the heating) were completely different, the main damage mechanism is very similar: crystallization to Mo_2N and outgassing of N_2, leading to bubble formation inside the multilayer structure. However the timescale of the damage processes (less than 1 microsecond vs. hours, for pulsed and continuous annealing, respectively) and the damage threshold temperatures (approx. 2023 K vs. 1063 K) are different. This is caused by the difference in the atoms mobility in solid and liquid phases; its value changes by many orders of magnitude when crossing the melting point.

The results show that MoN/SiN multilayer optics can be used at femtosecond XUV light sources for fluences up to 48 ± 7 mJ/cm^2 for p-polarized light (and even higher fluences for s-polarized light) under the condition that the repetition rate of the source allows the deposited heat to dissipate between subsequent pulses. The nature of the damage mechanism is melting of MoN layer and releases of gaseous nitrogen. Similarly, in the previously studied Mo/Si multilayers the damage threshold was determined by melting of the Si layers. The melting temperature of MoN is much higher than that of Si, but the observed damage threshold of MoN/SiN multilayers is similar to the damage threshold of the Mo/Si multilayers. This is caused by increased absorption and therefore enhanced temperatures in the MoN/SiN multilayers. However the MoN/SiN multilayers are more suitable for slow heating at extended temperatures compared to the Mo/Si case (below the dissociation temperature). The nature of the damage mechanisms allows for extrapolation of the results for other 4th generation light sources with pulses longer than those of FLASH.

Acknowledgements

Experiments at FLASH have been performed within the framework of the Peak-Brightness-Collaboration (project II-20022049 EC). Support from the PBC and the operators of the FLASH facility are gratefully acknowledged. This work has been partially carried out in the frame of the FOM Industrial Partnership Programme I10 (XMO) which is supported by Carl Zeiss SMT AG, Oberkochen and the `Stichting voor Fundamenteel Onderzoek der Materie (FOM)', the latter being supported by the `Nederlandse Organisatie voor Wetenschappelijk Onderzoek (NWO)'. Additional support via the AgentschapNL (EXEPT project) is acknowledged. This work has also been supported by the Ministry of Science and Higher Education of Poland, SPB nr. DESY/68/2007, the Czech Ministry of Education from the National Research Centers program (Projects LC510 and LC528) and program INGO (Grant LA08024), Czech Science Foundation (Grant 202/08/H057), by the Academy of Sciences of the Czech Republic (Grants Z10100523, IAA400100701, and KAN300100702) and by Lawrence Livermore National Laboratory under contract DE-AC52-07NA27344.

#136911 - $15.00 USD Received 20 Oct 2010; revised 9 Dec 2010; accepted 9 Dec 2010; published 22 Dec 2010
(C) 2011 OSA